JACS Au
AN OPEN ACCESS JOURNAL OF THE AMERICAN CHEMICAL SOCIETY

pubs.acs.org/jacsau
Article

Molecular Engineering of Sulfone-Xanthone Chromophore for Enhanced Fluorescence Navigation

Hong Zhang, Fei-Fan Xiang, Yan-Zhao Liu, Yu-Jin Chen, Ding-Heng Zhou, Yan-Hong Liu, Shan-Yong Chen, Xiao-Qi Yu, and Kun Li*

Cite This: JACS Au 2023, 3, 3462−3472
Read Online

ACCESS | Metrics & More | Article Recommendations | Supporting Information

ABSTRACT: Enriching the palette of high-performance fluorescent dyes is vital to support the frontier of biomedical imaging. Although various rhodamine skeletons remain the premier type of small-molecule fluorophores due to the apparent high brightness and flexible modifiability, they still suffer from the inherent defect of small Stokes shift due to the nonideal fluorescence imaging signal-to-background ratio. Especially, the rising class of fluorescent dyes, sulfone-substituted xanthone, exhibits great potential, but low chemical stability is also pointed out as the problem. Molecular engineering of sulfone-xanthone to obtain a large Stokes shift and high stability is highly desired, but it is still scarce. Herein, we present the combination modification method for optimizing the performance of sulfone-xanthone. These redesigned fluorescent skeletons owned greatly improved stability and Stokes shift compared with the parent sulfone-rhodamine. To the proof of bioimaging capacity, annexin protein-targeted peptide LS301 was introduced to the most promising dyes, J-S-ARh, to form the tumor-targeted fluorescent probe, J-S-LS301. The resulting probe, J-S-LS301, can be an outstanding fluorescence tool for the orthotopic transplantation tumor model of hepatocellular carcinoma imaging and on-site pathological analysis. In summary, the combination method could serve as a basis for rational optimization of sulfone-xanthone. Overall, the chemistry reported here broadens the scope of accessible sulfone-xanthone functionality and, in turn, enables to facilitate the translation of biomedical research toward the clinical domain.

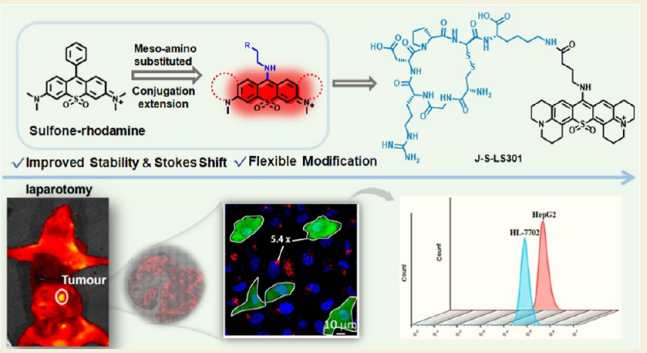

KEYWORDS: *sulfone-xanthone, molecular engineering, fluorescence navigation*

Fluorescence imaging technique has attracted more and more attention in the preclinical medical research, clinical−pathological examination, and modern biological domain.[1−5] As for the core of fluorescence imaging, small-molecule organic fluorescent dyes that own preeminent optical and chemical properties are urgently needed, which could ensure high fidelity and quality signal output. To be suitable for clinical use, the most critical characteristics for newly designed small-molecule organic fluorescent dyes are large Stokes shift, high fluorescence efficiency in the near-infrared region, sufficient stability, and ideal solubility for complete biodistribution and pharmacokinetics research.[6]

Regrettably, the three kinds of fluorescent dyes (indocyanine green, fluorescein, and methylene blue) that are widely used in the clinical range all suffer from obvious small Stokes shift and nonideal photostability.[7−9] Furthermore, for the range of biomedical research studies, the widely used rhodamine derivative emits photons in the visible spectrum region, which suffers from surface penetration depth and severe autofluorescence from biological tissues. Even though some of the rhodamine derivates were extended to the NIR-II region, the apparent bulky molecular structure caused nonideal solubility.[10−14] To solve the defect, it needs to encapsulate to form nanomaterials that broadly limit the sufficient biodistribution and pharmacokinetics study. Hence, it is obvious that only a few small-molecule fluorophores own the above optimal properties in all of these categories. The development of newly designed organic fluorescent dyes that addressed the above defects is highly demanded.

Among the numerous fluorescent dyes, rhodamine derivates play an important role in the foundational bioimaging experiment due to high fluorescent brightness. Since the first report on Si-substituted rhodamine analogues by Qian and co-workers, phosphine oxide, sulfone, and ketone moieties were introduced.[15−20] Based on this, a lot of novel NIR−NIR II

Received: October 10, 2023
Revised: November 7, 2023
Accepted: November 20, 2023
Published: December 8, 2023

emission rhodamine analogues are constructed.[21−25] It could be seemed as a flexible method through altering the C-10 bridging atom of the xanthene skeleton to lead the significant red shifts in absorbance and emission. However, the inherent defects of the rhodamine derivate, small Stokes shift, are still not solved. Much more importantly, with the electron-withdrawing ability of the C-10 bridging atom increased (silicon group, phosphorus oxide group and sulfone group), the stability of rhodamine fluorophores decreased, causing limited biomedical application, especially sulfone-rhodamine.[19,26−29] To increase the Stokes shift of rhodamine, Burgess and co-workers utilized the meso-amino-substituted method, and this kind of meso-amino-substituted rhodamine analogues still possess high fluorescent brightness of the original rhodamine skeleton.[30] Unfortunately, the meso-amino modification method could cause the hypsochromic shifts in their emission and absorption spectrum. Hence, based on this, the further method of altering the C-10 bridging atom is used to develop large Stokes shift NIR emission fluorescent dyes in Klán group's work, Hell group's work, Ahn group's work, and our previous work.[31−38] Nevertheless, among these studies, the emission wavelength of these redesigned meso-amino-substituted rhodamine derivatives was about 650 nm. The fluorescence emission wavelength over 700 nm with a large Stokes shift was still not reported.

To this end, in this article, we undertook a combination method to optimize the performance of sulfone-xanthone. The meso-amino-substituted and π-system-extending derivatives were utilized to construct a series of new fluorescent chromophores. Herein, as described in Scheme 1, we

Scheme 1. Rational Design of Meso-Amino-Substituted Sulfone-Xanthone Derivatives

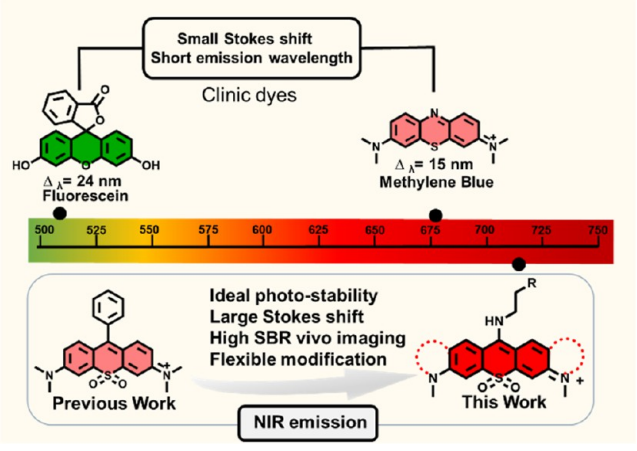

demonstrate that meso-amino-substituted sulfone-xanthone still possessed the high fluorescence efficiency of the parent skeleton, and the Stokes shift was greatly improved (>4070 cm^{-1}). J-S-ARh that owned the best combination optical properties was selected as the fluorescent platform for further testing of the bioimaging ability in vivo. J-S-ARh was conjugated with the annexin A2 protein-targeted cyclic octapeptide to form probe J-S-LS301. Probe J-S-LS301 could not only distinguish cancer cells and normal cells in the mix-cultured model but also accurately identify the hepatocellular carcinoma tissue. The results could completely match the results of pathological analysis, which displayed the characteristic of simplifying the tumor diagnosis. This study reports the longest emission wavelength (>700 nm) in the range of meso-amino-substituted rhodamine substrates with large Stokes shift (>4070 cm^{-1}) and high fluorescence efficiency. It adds an essential small-molecule dye category to classical dyes and provides a new fluorescence tool for in vivo fluorescence imaging.

RESULTS AND DISCUSSION

Theoretical Basis and Design Strategy

In this work, our aim is to develop highly stable and large Stokes shift sulfone-xanthone derivatives. According to the previous work, to achieve improved stability and Stokes shift in the parent sulfone-rhodamine skeleton, the key is to decrease the electrophilicity at the C7−C8 position of the sulfone-rhodamine skeleton.[31−33] We first identified the role of the meso-amino group substituted at the C7 position in dimethylamino-xanthene-derived scaffolds (Figure 1a). Computational calculations using multifin were performed for meso-amino-substituted sulfone-xanthone according to the previous method.[39,40] As shown in Figure 2a, the Mulliken charge on the C7 position of SRh was +0.644 au, whereas that of M-S-ARh was +0.702 au. It was quite apparent that the electrophilicity at the C7 position of the modified chromophore was significantly lowered in the modified chromophore compared to that in the parent skeleton. However, the previous work reported that the meso-amino-substituted derivative could cause an obvious hypochromatic shift that was adverse for the sufficient depth of tissue penetration.[30] To this end, we further analyzed the electronic excitation of these newly designed dyes. As shown in Figure 1b, these dyes displayed gradually increased LUMOs and increased HOMOs except for compound I-S-ARh. In addition, the energy gap (Eg) of HOMO−LUMO showed an obvious tapering characteristic (2.904−2.756 eV), which matched well with the absorption bathochromic shift trend observed from UV−vis−NIR spectra. This could be explained by the modification of arylamine in the fluorescent skeleton and the extension of the π-system.

Synthesis of S-ARhs and Photophysical Properties

To verify that the combination design method could improve the stability and Stokes shift that form the high-performance NIR emission fluorescent dyes, we constructed these new meso-amino-substituted sulfone-xanthone derivatives. These newly designed fluorescent dyes were synthesized in six steps with acceptable yields. All of the synthetic details and other characterization data are shown in the Supporting Information (Schemes S1−S6 and Figures S19−S35).

With these S-ARhs in hand, the optical properties of these dyes were first tested. As shown in Figure 1c−i, M-S-ARh, P-S-ARh, N-S-ARh, J-S-ARh, and I-S-ARh showed a maximum absorption peak at 505, 514, 522, 542, and 544 nm, respectively. In addition, due to the similar structure of the skeleton, all of these compounds possessed a shoulder peak at 350−430 nm. In addition, S-ARhs all obeyed the Lambert−Beer law in the range of 1−10 μM in PBS (Figure S1) and thus displayed the ideal water solubility for imaging in a practical biomedical field. In addition, according to the Lambert−Beer law, the molar absorption coefficients of S-ARhs were tested around 1.08×10^4 to 3.99×10^4 M^{-1} cm^{-1}, which still possessed the ideal property of the original sulfone-rhodamine.

The fluorescence emission wavelengths of these dyes were tested subsequently. As shown in Figure 1g, the wavelengths

https://doi.org/10.1021/jacsau.3c00613
JACS Au 2023, 3, 3462−3472

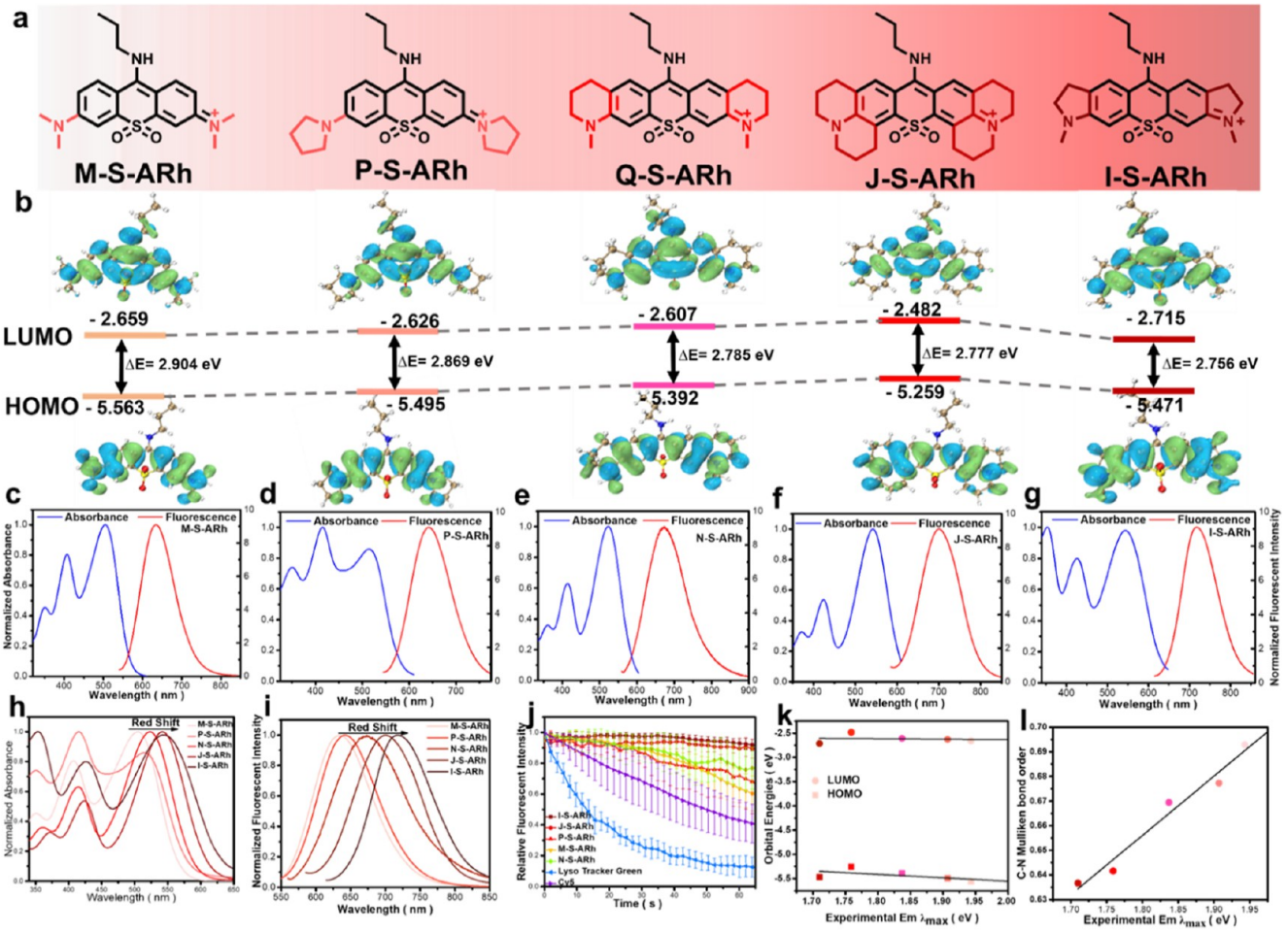

m

Compound	λ_{abs} (nm)	λ_{em} (nm)	SS (cm^{-1})	ε ($M^{-1}cm^{-1}$)	Φ_{fl} (%) PBS	DCM	MeOH
M-S-ARh	505	638	4130	3.11×10^4	14.66	30.73	25.15
P-S-ARh	514	650	4070	1.39×10^4	17.38	42.85	34.47
Q-S-ARh	522	675	4340	3.99×10^4	15.57	10.38	81.24
J-S-ARh	542	705	4260	3.64×10^4	15.44	30.03	27.58
I-S-ARh	544	725	4590	1.08×10^4	2.15	16.94	7.08

Figure 1. (a) Structure of the S-ARh derivates. (b) Frontier orbitals and energy levels of the S-ARhs derivates calculated by DFT at the B3LYP/6-31+G(d,p) level of Gaussian 09. (c−g) Normalized absorption and emission spectrum of M-S-ARh, P-S-ARh, N-S-ARh, J-S-ARh, and I-S-ARh, respectively, in PBS solution pH 7.4 at 25 °C. (h) Normalized absorption spectrum of the S-ARh derivates. (i) Normalized fluorescence spectrum of the S-ARh derivates. (j) Photostability of S-ARhs. (k) Correlation between the experiment emission wavelength, λ_{em}, and HOMO−LUMO orbital energies. (l) Correlation (R^2 = 0.97) between the signed C−N bond and Mulliken bond order in HOMO and the experiment emission wavelength, λ_{em}. (m) Optical properties' summary of S-ARhs dyes.

were at 648, 653, 675, 705, and 725 nm. The obvious bathochromic shift phenomenon could be observed with the π-system extended in the skeleton. Furthermore, the fluorescence spectrum in MeOH and aprotic solvents DCM and DMSO were also investigated (Figure S2). Obvious solvent effects could be observed as a significant bathochromic shift with increased solvent polarity. Based on the spectrum data, Stokes shifts were calculated as 4130, 4070, 4340, 4260, and 4590 cm^{-1}. The Stokes shifts were larger than the previous reports of sulfone-rhodamine derivates (Table S1).[19,25,26,32] Furthermore, it was reported that rhodamines derivates owned the pH sensing characteristic.[5,31,32] Hence, the fluorescence intensities of these dyes were also tested at different pHs. As shown in Figure S3, all of the reconstructed dyes showed gradually decreased emission intensities in the pH range from 6 to 8. The pH-sensitive characteristic of these dyes could be

https://doi.org/10.1021/jacsau.3c00613
JACS Au 2023, 3, 3462−3472

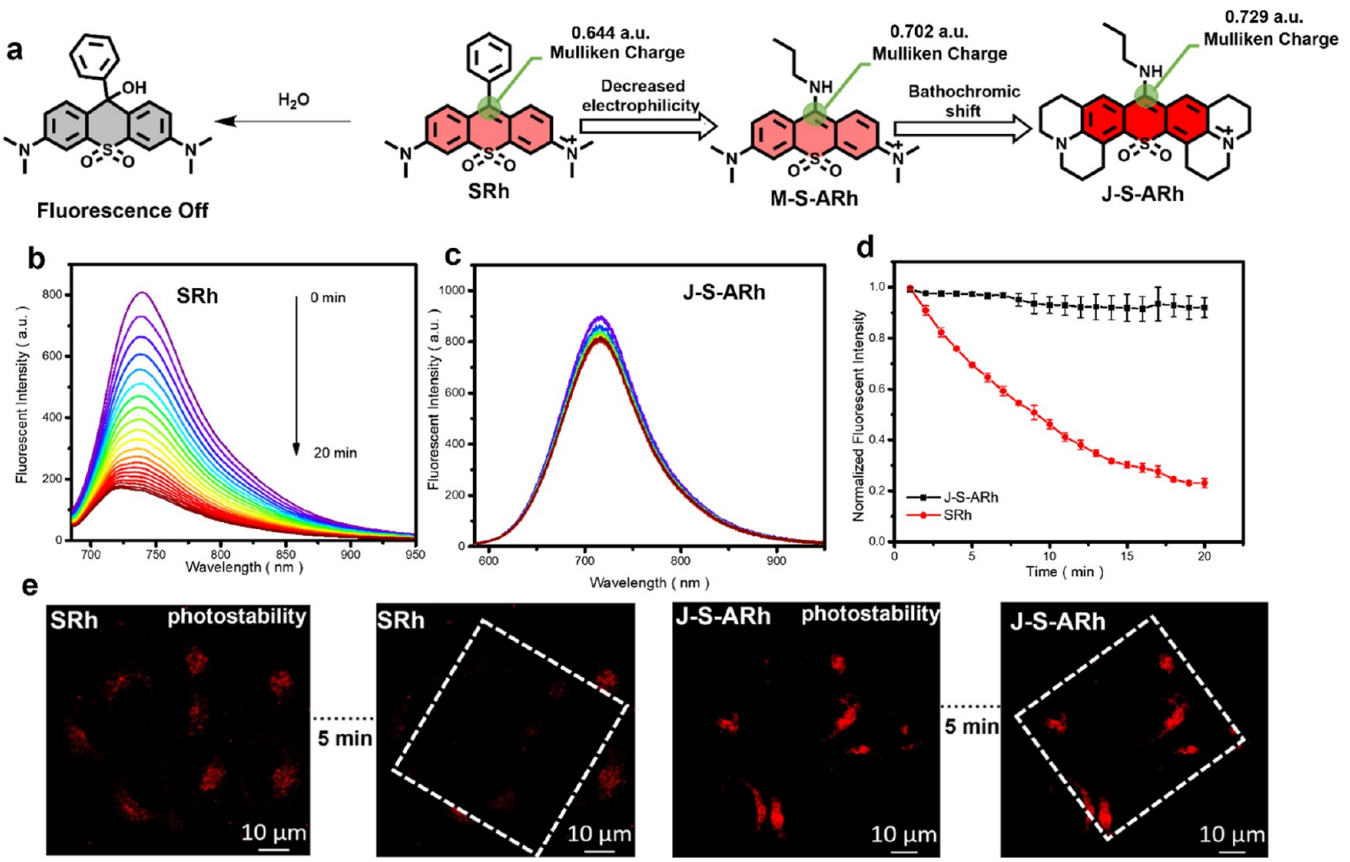

Figure 2. (a) Schematic presentation of the instability in PBS buffer of SRh and the improved stability of the S-ARh derivatives. (b,c) Normalized fluorescence spectrum of SRh (5 μM) and J-S-ARh (5 μM), respectively, in PBS solution pH 7.4 at 25 °C. (d) Normalized fluorescence time curves of SRh and J-S-ARh. (e) Photostability of SRh (1 μM) and J-S-ARh (1 μM) in living cells.

explained by the protonation and deprotonation process under the different solution. As shown in Figure S4, the imine form was nonfluorescent, and it was protonated to form the high-fluorescent enamine form in the acidic solution. Hence, it could be utilized as a kind of pH response fluorescent probe. Subsequently, the fluorescence quantum yield of these dyes was measured. The highest absolute fluorescence quantum yield could reach 17.38 in PBS and even 81.24 in EtOH. The high brightness characteristics were enough for further fluorescence imaging applications.

Indeed, the further quantified C−N bond orders in HOMOs correlate well with the experimental emission energies (Figure 1k−l), and it showed an obvious decreased tendency, indicating that emission energies are lowered as the aryl-amine-group π-electronegativity increases.

After the basic optical properties were sufficiently investigated, the stability of these newly designed fluorescent dyes was further studied. It is known that the C7 position of sulfone-rhodamine is more susceptible to nucleophilic attack compared to that of the Si-substituted and phosphorus-substituted rhodamine dyes.[5,19,33] Even in the PBS buffer, H_2O could also attack the sulfone-rhodamine skeleton due to fluorescence quenching, which limited further application.[19] To this end, we tested the stability in the PBS buffer of these reconstructed S-ARh derivates. As shown in Figure 2a−d, as time went on, sulfone-rhodamine displayed obvious fluorescence quenching, which represented the apparent unstable characteristic. On the contrary, the redesigned meso-amino-substituted sulfone-xanthone derivates owned the improved stability, which could avoid the attack of H_2O. Furthermore, the GSH stability of SRh and S-ARh derivates was also tested. As shown in Figure S5, SRh showed obvious fluorescence quenching after GSH was added to the testing buffer. However, after introducing the propylamine unit, the fluorescence of these redesigned dyes was almost not affected, which displayed obvious enhanced stability in the presence of GSH. From the structural stability point of view, it could be explained by the strong electron-withdrawing sulfone moiety causing an enhanced electrophilic property toward nucleophilic attack, and the electron-donating propylamine decreases the electrophilicity. Subsequently, the photostability of SRh and S-ARh derivatives in living cells was investigated. It is shown in Figures 2d and S6 that only M-S-ARh displayed slightly photobleaching feature; the other fluorophores possessed high photostability.

Bioimaging Applications

As for the basic prerequisite of the bioimaging application, the cytotoxicity of these fluorescent dyes must be investigated well to not perturb the normal cellular process. Hence, the standard CCK-8 assays were carried out to assess the cytotoxicity. As shown in Figures S7 and S8, when the HepG2 cells were incubated for 1.25−5 μM S-ARhs for 24 h, the cell viability was more than 80% except for the P-S-ARh and I-S-ARh. These results indicated the ideal biocompatibility of M-S-ARh, N-S-ARh, and J-S-ARh.

Subsequently, we tested the subcellular localization of these dyes. As shown in Figure S9, all of the stained structures possessed the typical lysosomal morphology, and the Pearson

https://doi.org/10.1021/jacsau.3c00613
JACS Au 2023, 3, 3462−3472

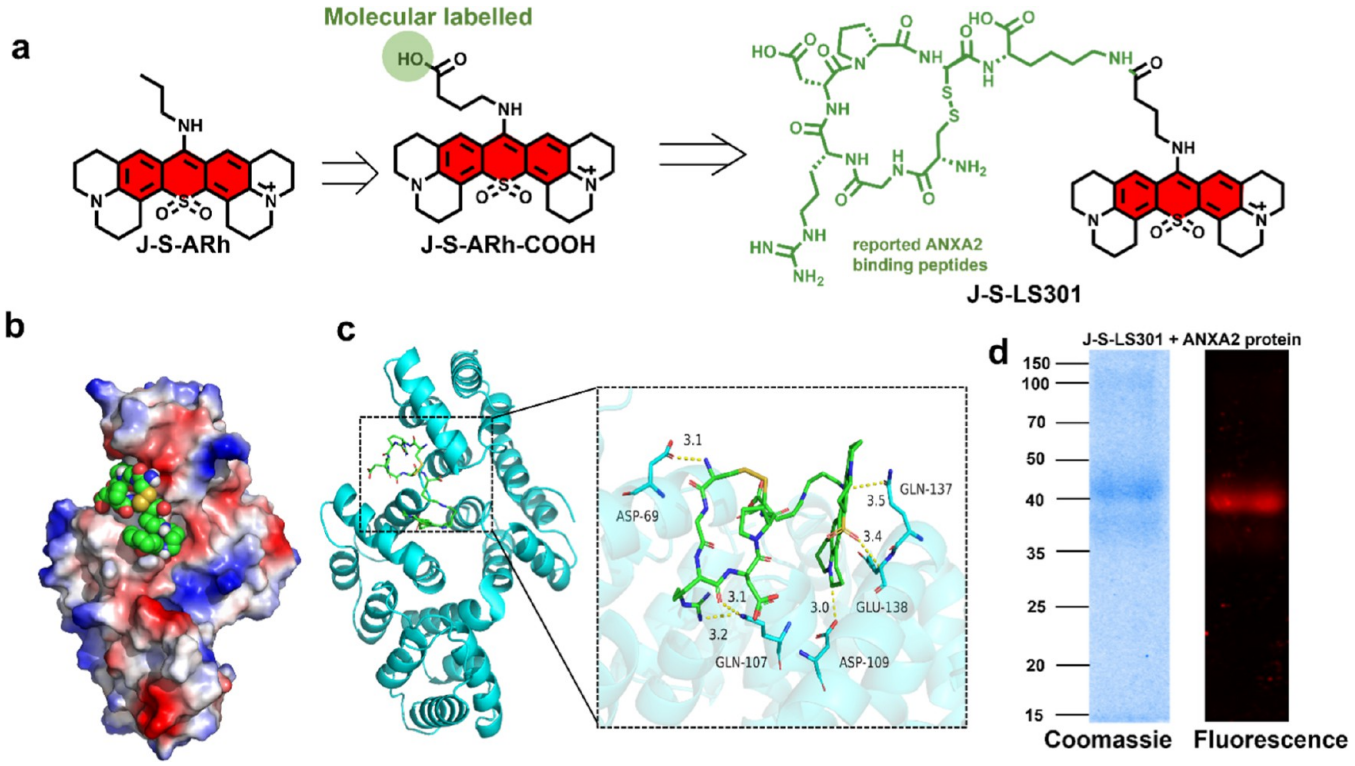

Figure 3. (a) Structure of the reported ANXA2 binding peptide and fluorescent dye J-S-ARh-COOH with the labeled site. (b) Electrostatic surface of ANXA2. (c) 3D structure and the binding mode of the complex and the binding region of the complex. (d) Gel electrophoresis binding results of J-S-LS301 to ANXA2. J-S-LS301 (5 μL, 10 μM) were incubated with 1 μg recombinant ANXA2 recombinant protein.

colocalization coefficients were calculated as 0.87, 0.93, 0.86, 0.87, and 0.89, respectively. To verify the lysosomal stained mechanism, Bafilomycin A1 (Baf-A1, a kind of inhibitor of V-ATPases that could inhibit the lysosomal acidification process) was used to increase the pH value of lysosomes. As shown in Figure S10, the fluorescent signal of the group that pretreated with Baf-A1 did not exhibit the lysosomal morphological feature, and it could demonstrate the pH-dependent staining mechanism of these fluorophores. The results were matched with the pH-intensity-dependent fluorescence data shown in Figure S3, which indicated that the probe was suitable for the lysosome imaging.

To the proof of bioimaging capacity, we utilized J-S-ARh which owned the best combination optical properties as the fluorescent platform to test the capacity for the biomolecule labeling. The 4-aminobutyric acid was introduced to the skeleton as shown in Figure 3a; ANXA2 was proved as a kind of calcium-dependent phospholipid-binding proteins that belong to the member of the annexin protein family.[41] It is a widely studied protein because of the cancer-associated PTM.[42] It is upregulated in many cancers including breast, colon, liver, pancreatic, and brain tumors, suggesting that it has a key function in tumor proliferation, angiogenesis, invasion, and metastasis.[42−47] In 2020, Samuel and co-workers described a cyclic octapeptide that could bind the ANXA2 protein and thus as a useful reporter for the pANXA2-positive cancer cells.[48] Hence, J-S-ARh-COOH was utilized to link the cyclic octapeptide, LS301, to realize the high-fidelity tumor imaging. After being synthesized, the pH-sensitive experiment of this probe was tested. It is shown in Figure S11 that the fluorescent signal was not affected from pH 4−pH 7.5 and could be used for tumor imaging. Furthermore, molecular docking of probe J-S-LS301 and targeted protein ANXA2 was performed. As shown in Figure 3b,c, the results of molecular docking showed that the probe possessed a good binding effect and high matching degree (binding energy −8.10 kcal/mol) with the targeted ANXA2. The selected conformation with the lowest energy according to the score reveals the binding mechanism of the probe and ANXA2. The complexes formed by the docked compounds and ANXA2 were visualized using Pymol2.1 software to obtain the binding pattern of the compounds and ANXA2. Based on the binding pattern, it could be observed that J-S-LS301 could form hydrogen bonds with residues of ASP-109, GLN-137, GLU-138, GLN-107, and ASP-69, with short distance and strong binding ability, making important contributions to stabilize the probe. In addition, according to Figure 3b, it can be found that small molecules match well with protein cavities. We next used in vitro binding experiments of the human recombinant ANXA2 proteins and J-S-LS301, and in Figure 3d, gel electrophoresis assays clearly showed the binding ability of ANXA2 proteins with the probe.

Subsequently, we chose HepG2 cells, A549 cells, and NCI-H460 cells to assess the time of the internalization. As shown in Figure S12, cancer cells were pretreated with J-S-LS301 and incubated for 15 min, 2, and 6 h. The group of 15 min could observe only the weak fluorescent signal, which represented the relatively low uptake. As for the 2 and 6 h groups, the much more intense fluorescent signal could be detected. Hence, for the further cellular imaging experiment, J-S-LS301 was incubated for 2 h to ensure sufficient cellular uptake. In order to verify the ANXA2 binding ability of J-S-LS301 which could facilitate the uptake of cancer cells, we used probe J-S-LS301 and the fluorescent skeleton without the binding peptide to test the imaging ability in diverse cancer cells. As

https://doi.org/10.1021/jacsau.3c00613
JACS Au 2023, 3, 3462−3472

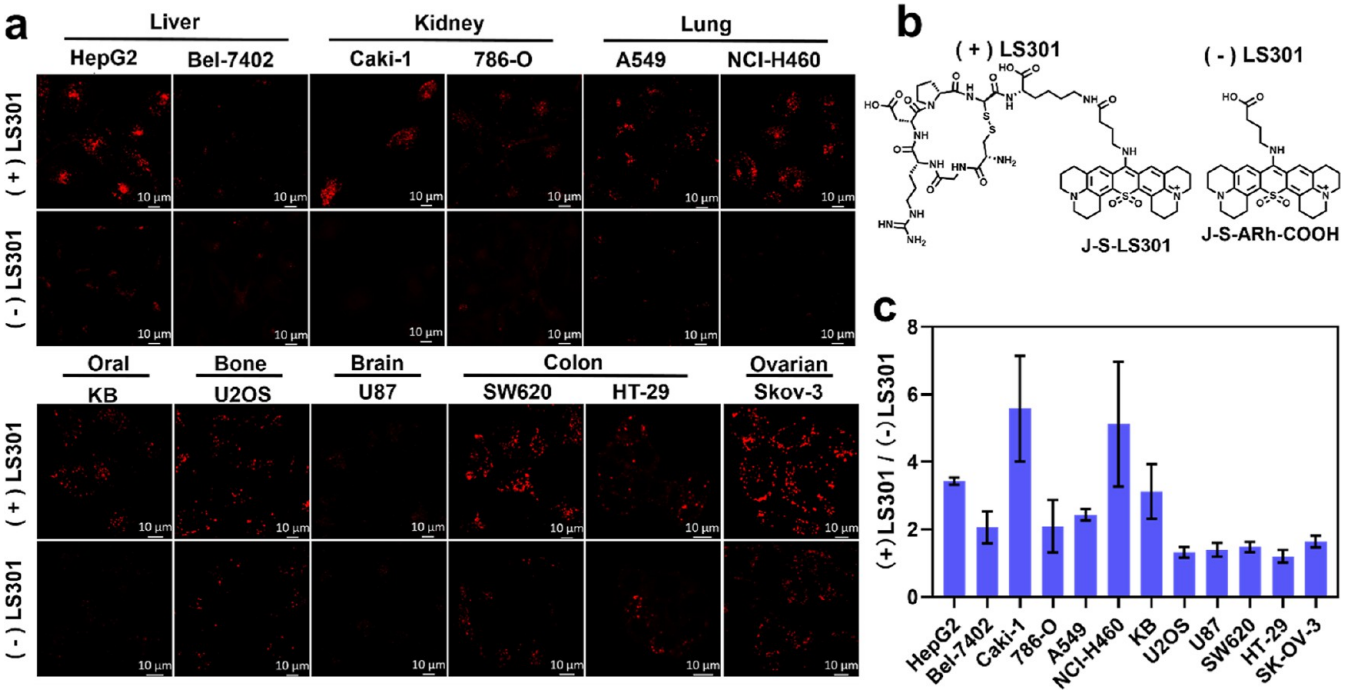

Figure 4. (a) Assessment of cellular uptake of J-S-LS301 and J-S-ARh-COOH in different cancer cell lines. All the concentrations of probes were 10 μM and stained at 37 °C for 2 h. (b) Structure of targeted probe J-S-LS301 and comparison compound J-S-ARh-COOH. (c) Ratio of the uptake counted by the relative fluorescence intensity between the J-S-LS301-stained group and the fluorescent skeleton-stained group.

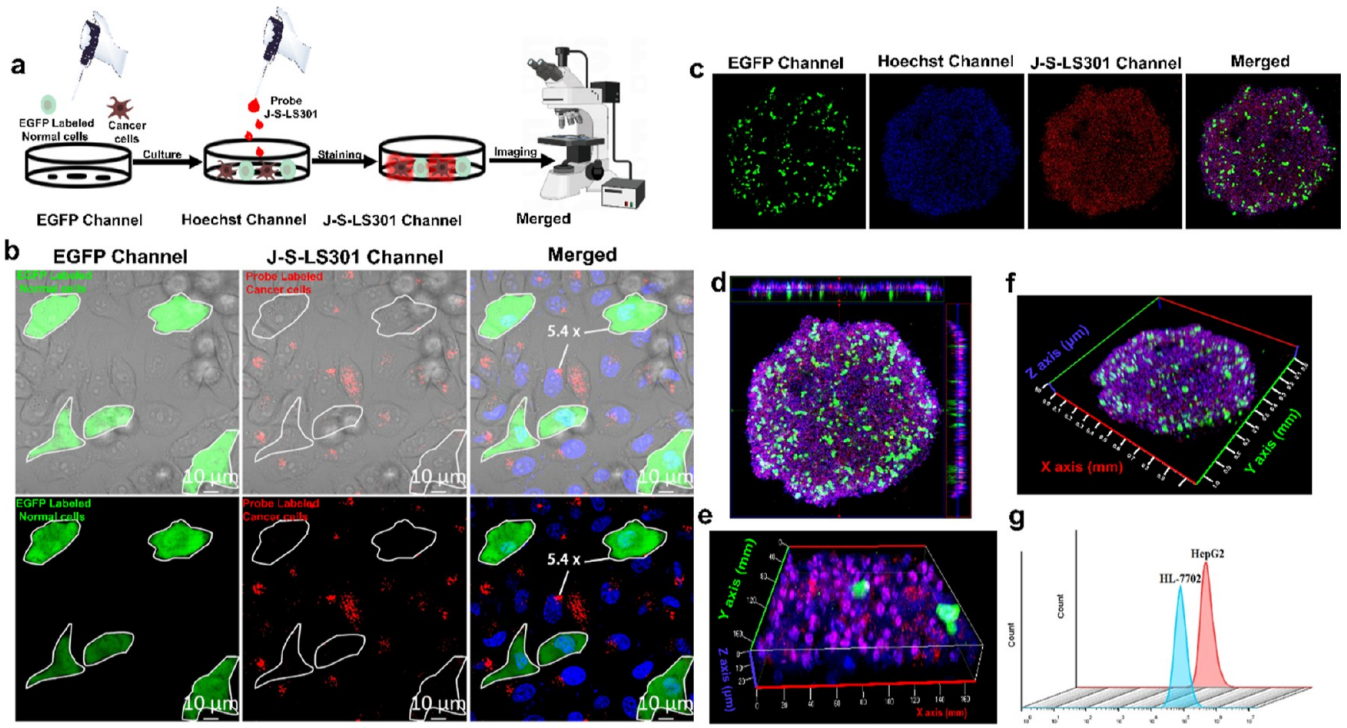

Figure 5. (a) Schematic presentation of probe J-S-LS301 to distinguish the cancer cells in the mix-cultured cancer−normal cell models. (b) Fluorescent images of mix-cultured EGFP-transfected HL-7702 cells and HepG2 cells; the green signal was the EGFP fluorescence; the red signal was the J-S-LS301 fluorescence (10 μM) and stained at 37 °C for 2 h; and the blue signal was the Hoechst-33342 fluorescence (10 μg/mL) and stained at 37 °C for 30 min. (c) Fluorescent images of mix-cultured HL-7702 cell and HepG2 cell 3D tumor spheroids. (d) Cross-sectional images of the *x*- and *y*-axes of the mix-cultured 3D tumor spheroids. (f) 3D reconstructed images of the mix-cultured 3D tumor spheroids (taken by the 10× objective lens). (e) 3D-reconstructed images of the mix-cultured 3D tumor spheroids (taken by the 63× objective lens). (g) Flow cytometric analysis of J-S-LS301 fluorescence intensity in HL-7702 cells and HepG2 cells.

shown in Figure 4a, 12 kinds of cultured cancer cell lines were both imaged; only Bel-7402 cells and U87 cells did not show the obvious elevated uptake, all other cancer cell lines showed higher fluorescence intensity than the fluorescent skeleton-

https://doi.org/10.1021/jacsau.3c00613
JACS Au 2023, 3, 3462−3472

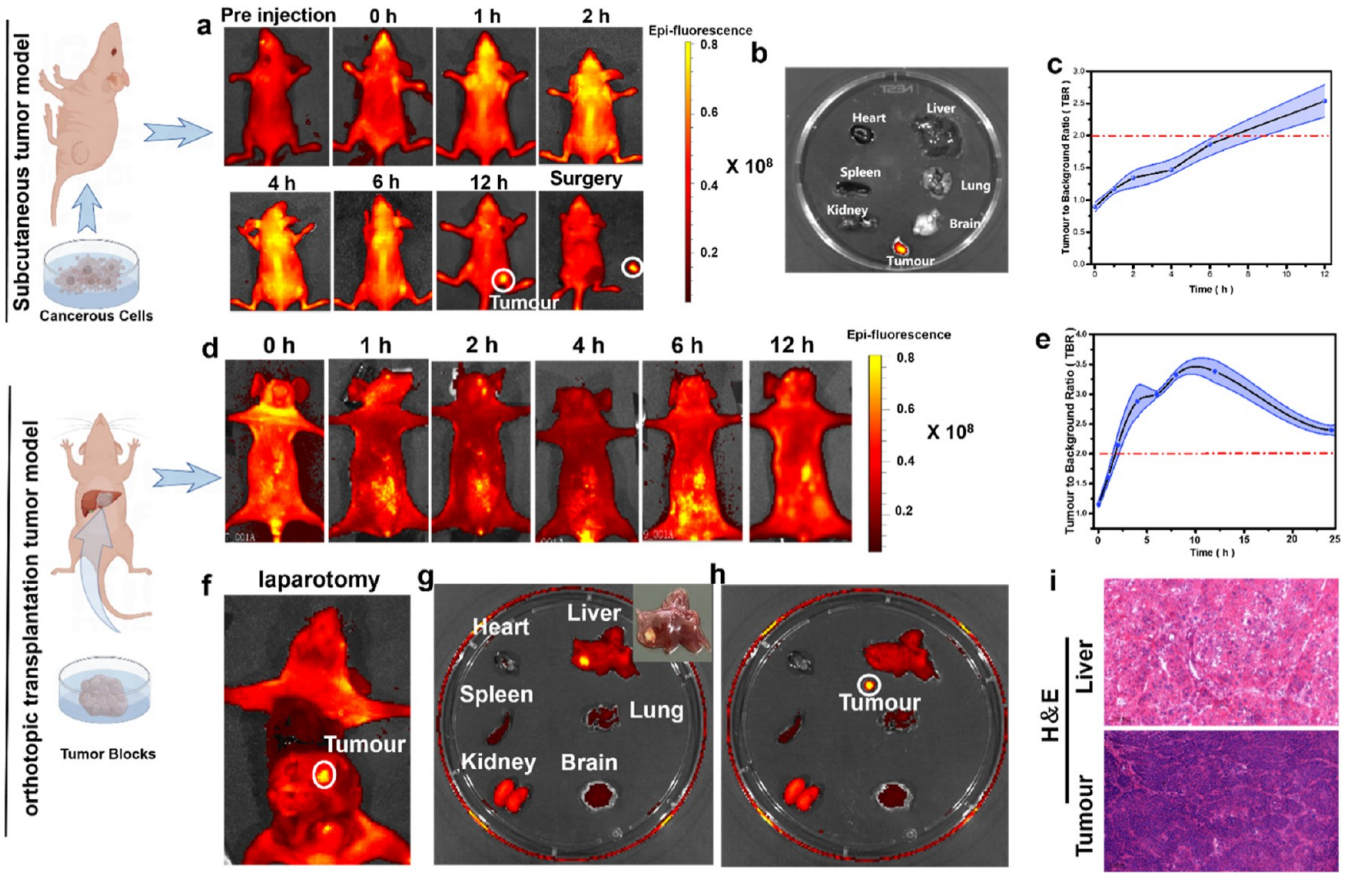

Figure 6. (a) Fluorescent images of subcutaneous xenotransplanted tumor-bearing nude mice at the indicated time points after i.v. administration of J-S-LS301. (b) Fluorescent images of the organ biodistribution of subcutaneous xenotransplanted tumor-bearing nude mice. (c) Quantitative time−course assessment of TBR of subcutaneous xenotransplanted tumor-bearing nude mice. (d) Fluorescent images in vivo at different time points after probe J-S-LS301 (5×10^{-4} M, 100 μL, in 5:95 DMSO/saline, v/v) was injected to the liver-tumor bearing nude mice models through the tail vain. (e) Relative fluorescent tumor-to-background ratio counted through the fluorescent images in vivo; error bars represent SD. (f) Fluorescent images of the laparotomy of liver-tumor-bearing nude mice after injecting the probe for 24 h. (g) Fluorescent images of typical ex vivo biodistribution of the representative organs. (h) Fluorescence-guided tumor excision from the ex vivo liver. (i) H&E-stained results of the normal liver tissues and the resected tumor.

stained group. Furthermore, the relative fluorescence intensity in different cancer cell lines was counted and is shown in Figure 4c; it could be seen that HepG2 cells, Caki-1 cells, NCI-H460 cells, and KB cells possessed a relatively high ratio of the uptake, which may represent the relatively high expression of ANXA2 proteins in these cancer cell lines. All these results indicate that the synthesized probes, J-S-LS301, could internalize into the cancer cell lines and thus is a promising candidate for fluorescence imaging agent for accurate tumor imaging and the screening of pro-drug for the upregulated ANXA2 activities in cancer tissues in the clinical context.

It is clear that the upregulated ANXA2 in cancer cells could elevate the uptake of J-S-LS301. Hence, we further evaluated the distinguishing abilities of cancerous cells and normal cells of the probe. For this purpose, the mix-cultured cancer−normal cell models were constructed. As shown in Figure 5a, for easy identification of the normal cells in the mix-cultured cell models, the normal cells were transfected with EGFP to emit the obvious green fluorescent signal. Then, the mix-cultured cells were stained by the probe, J-S-LS301, to perform fluorescence imaging. The HL-7702/HepG2 mix-cells were constructed first. To our delight, the probe displayed excellent characteristics for specific lighting of the cancer cells in the mix-cultured models, which could be seen in Figure 5b; there were almost no red fluorescent signal in the normal cells, which exhibited the intense green fluorescent signal; however, cancer cells HepG2 showed the intense red fluorescent signal. Nevertheless, the monolayer cells could not represent the typical complexity of tumors, 3D-structured spheroids, as a valid intermediate between the monolayer in in vitro cells and in vivo tissue, and are heterogeneous cell aggregates that have been applied to study the multicellular aggregation of tumors and avascular metastasis in vivo.[49] Hence, mix-cultured 3D-structured spheroids were constructed. As shown in Figure 5c−e, the red fluorescent signal in the HL-7702 cells was very weak, and the red fluorescence intensity in the HepG2 cells was extremely strong, and the fluorescence intensity was detected from the spheroid up to 126 μm, which illustrates the deep tissue penetration capability of J-S-LS301. Furthermore, in order to test the universality of the cancerous cellular identification ability, we also constructed the mix-cultured HEK-293/Caki-1 cells and 3D-structured spheroids. As shown in Figures S13−S15, the same as the results of mix-cultured HL-7702/HepG2 cells, J-S-LS301 still performed well in distinguishing cancer cells. There was almost no red fluorescence in the normal cells. That is, the excellent cancerous cellular imaging ability was fully demonstrated,

https://doi.org/10.1021/jacsau.3c00613
JACS Au 2023, 3, 3462−3472

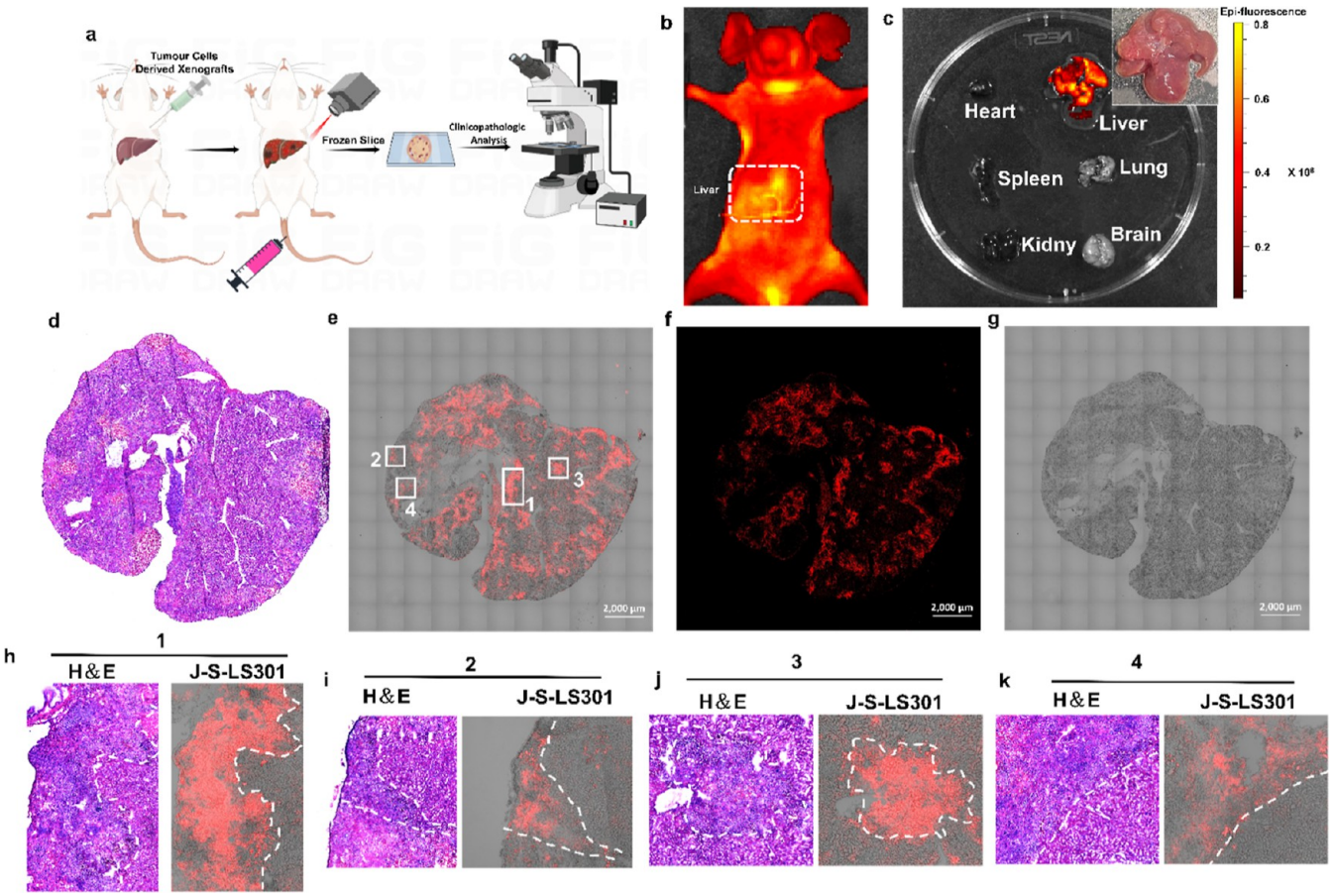

Figure 7. (a) Schematic presentation of the construction of the cell-derived xenograft hepatocellular tumor model and the imaging process of J-S-LS301 in tumor recognition. (b) Ex vivo fluorescent image of the mice after intravenous injection of J-S-LS301 (5×10^{-4} M, 100 μL, in 5:95 DMSO/saline, v/v) for 12 h. (c) Fluorescent images of typical ex vivo biodistribution of the representative organs. (d) H&E staining results of the frozen slice prepared from the resected liver. (e,f) Fluorescent images of the frozen slice prepared from the resected liver. (g) Bright images of the frozen slice prepared from the resected liver. (h–k) Enlarged region of the H&E staining images and the fluorescent images.

and according to the results, it could be utilized as for a powerful tool for the cancerous cellular identification.

Benefiting from the excellent fluorescence imaging ability of J-S-LS301 in the cell, the further evaluation of tumor fluorescence imaging in vivo was administered. We constructed the subcutaneous tumor model in nude mice, as shown in Figure 6a–c; probe J-S-LS301 was injected through the tail vein, and the fluorescent images were collected. In vivo fluorescence imaging revealed the gradually accumulated process of J-S-LS301 within 24 h, and the fluorescent signal in the normal tissues was diminished gradually. The mice were euthanized to perform ex vivo organ fluorescence imaging. It could be obviously observed that substantial probe accumulation in the solid tumor tissues caused the intense fluorescent signal. On the contrary, a relatively low uptake and retention were displayed in other organs such as the heart, brain, spleen, and lungs. In addition, excretory organs such as the liver and kidneys showed relatively higher fluorescence intensity (1.678×10^7) than other organs but obviously lower than the tumor (5.729×10^7, shown in Figure S16). It could be explained by the metabolized process of J-S-LS301 in vivo. Hence, to study the biodistribution of J-S-LS301, normal Blab/c nude mice were tested. As shown in Figure S17, the fluorescent images of the major organ showed that J-S-LS301 was mainly metabolized through the kidney and liver. J-S-LS301 is a small fluorescent molecule, which showed obvious variable retention in the excretory organs such as the liver and kidneys. With the consideration that the subcutaneous tumor model could not mimic the real pathophysiology of cancer, we constructed the orthotopic transplantation tumor model of hepatocellular carcinoma. HepG2 cells were transplanted to the axilla of the right limb. The tumors were cut into 2–3 mm^3 sections and retransplanted to the liver to establish the orthotopic hepatocellular tumor model. Upon tumor formation, mice were used for fluorescence imaging. Probe J-S-LS301 was also injected to the tail vein, as shown in Figure 6d,e; the fluorescence intensity in the tumor region was gradually enhanced. The tumor-to-background ratio gradually increased. It reached the maximum, around 3.3 after 12 h postinjection, followed by the decreased TBR ratio as time went on. These in vivo biodistribution studies indicated that 12 h postinjection was the ideal time for fluorescence-guided tumor surgery. Hence, laparotomy was performed, as shown in Figure 6g,h; the tumor was clearly lighted by J-S-LS301. It exhibited the ideal TBR ratio for fluorescence-guided tumor surgery. Moreover, the major organs were excised for ex vivo fluorescence imaging. Only in the tumor could be detected the strong fluorescent signal, which represented the superior targeted characteristic for the cyclic octapeptide. Meanwhile, the hematoxylin–eosin (H&E) stain pathological analysis was executed to prove the tumor identity results in vivo (Figure 6i).

https://doi.org/10.1021/jacsau.3c00613
JACS Au 2023, 3, 3462–3472

Encouraged by the ideal fluorescence imaging results in the cancerous lump transplanted orthotopic hepatocellular tumor model, cancer cell-derived xenografts were carried out to construct the multinodular orthotopic hepatocellular carcinoma. As shown in Figure 7, probe J-S-LS301 was injected for 12 h, and the liver region of mice could observe a strong fluorescent signal. Furthermore, ex vivo organ fluorescence imaging showed the inhomogeneous fluorescent signal in the liver region, which should represent the multinodular tumor region. To prove the accuracy of J-S-LS301 in identifying this kind of multinodular tumor tissue, the liver tissues of the mice were prepared for frozen sections. The current gold standard pathological analysis of tumor tissues in tumor surgery was carried out, as shown in Figure 7d–f, the fluorescent signal displayed in several areas of the liver, and the H&E staining results also displayed the corresponding results; these areas owned the irregular cell arrangement shape and an obvious much more darker bluish-purple color. Much more importantly, the enlarged images of fluorescence and H&E results showed highly analogous results; the fluorescent region in the liver-frozen slice could match the results of pathological analysis in the H&E staining images. It indicated that probe J-S-LS301 could be of value for accurately identifying various malignant lesions of the liver, and our probe can clearly distinguish these lesions from normal tissue regions.

CONCLUSIONS

As the most widely used premier type of small-molecule fluorophores, rhodamine dyes have caught great development owing to their high brightness and flexible modification characteristic. Nevertheless, among the palette of rhodamine fluorophore, the longer emission wavelength sulfone-rhodamine still suffered from nonideal stability, which caused limited biomedical application. To this end, based on the study of meso-amino-substituted rhodamine, we have developed the combination method by incorporating the amino group into the structure at the meso-position and extending the π-system, yielding the meso-amino-substituted sulfone-xanthone derivatives. These new designed organic fluorescent dyes display a lower band gap, contributing to a larger Stokes shift of about 4070–4590 cm^{-1} than that of a traditional sulfone-rhodamine skeleton (<1000 cm^{-1}). Both the substituents and steric hindrance effect play an essential role in the spectroscopic properties of the dyes. Especially, J-S-ARh owned the ideal fluorescence quantum yields and longer fluorescence emission wavelength, which shows the great potential on the fluorescence imaging in vivo. For the further imaging capability study, the J-S-ARh skeleton was modified with cyclic octapeptide LS301. Probe J-S-LS301 could high fidelity identify the tumor cells and normal cells because of the different cellular uptake caused by the different expression of ANXA2 proteins. In addition, J-S-LS301 exhibited the specific strong fluorescent signal on tumors in the subcutaneous tumor model and the orthotopic transplantation tumor model of hepatocellular carcinoma. For the multinodular orthotopic hepatocellular carcinoma, J-S-LS301 could also identify the boundaries between the tumor tissues and normal tissues, which could match the results of the gold standard pathological analysis of H&E staining. Hence, J-S-LS301 could be utilized for accurate tumor imaging, fluorescence navigation surgery, and the frozen tissue slice identification to identify the tumor boundaries and reduce surgical trauma.

In summary, based on the combination methods, these new fluorescent dyes addressed the inherent defects, small Stokes shift, and nonideal stability of sulfone-rhodamine. In addition, the biomolecular labeling ability of the fluorescent platform was proved by modifying the tumor-targeted cyclic octapeptide, LS301. It showed specific and strong targeted fluorescent tumor imaging ability, confirmed by the optical imaging of the orthotopic transplantation tumor model of hepatocellular carcinoma and multinodular orthotopic hepatocellular carcinoma. It showed great promise in the biomedical reach field and could be a useful tool for fluorescence tumor surgical navigation.

METHODS

Materials

Unless otherwise noted, all chemical reagents were purchased from commercial suppliers and used without further purification. The detailed synthesis route could be found in the Supporting Information. All solvents were dried according to the standard methods prior to use.

Synthesis

The transformation of ketone into amino derivative was synthesized through general methods. The compound ketone (1 mmol) was dissolved in 20 mL of DCM, and oxalyl chloride (10 mmol) was added dropwise to the solution and stirred at room temperature for 12 h. Then, the solution was concentrated under vacuum. Subsequently, the residue was dissolved in 5 mL of DCM, and it was added dropwise to the solution of propylamine (25 mmol). The solution was stirred at room temperature for 30 min, and then the solution was concentrated under vacuum. The residue was purified by column chromatography on silica gel (DCM: MeOH) to afford the target product.

Analysis and Characterization

In the optical spectroscopic studies, all of the solvents were of either HPLC or spectroscopic grade. Thin-layer chromatography (TLC) was performed on silica gel plates, and spots were visualized under UV light. Column chromatography was carried out using 200–300 mesh silica gel (Qingdao Ocean Chemicals). NMR spectra were recorded on a Bruker AMX-400 spectrometer at 25 °C (^{1}H NMR: 400 MHz, ^{13}C NMR: 101 MHz), and chemical shifts (λ) are expressed in parts per million (ppm) using internal standard tetramethylsilane or the deuterated solvent ($CDCl_3$, CD_3OD) as reference. High-resolution mass spectrometry (HRMS) spectra were obtained on a Finnigan LCQDECA. The pH values were determined by a pH-3c digital pH meter (Shanghai Lei Ci Device Works, Shanghai, China) with a combined glass-calomel electrode. UV absorption spectra were recorded on a Persee TU-1901 UV–visible spectrophotometer. Fluorescence spectra were recorded on a Hitachi F-7000 fluorescence spectrophotometer. Cell imaging was performed on a Zeiss LSM 780 confocal laser scanning microscope.

Cell Culture

All cells were maintained at 37 °C in 5% CO_2. HepG2 and U87 were cultured in Dulbecco's modified Eagle's medium (DMEM) supplemented with 10% fetal bovine serum (FBS, Gibco) and 1% penicillin–streptomycin solution. Bel-7402, NCI-H460, SKOV-3, A549, SW620, Caki-1, and HL-7702 were cultured in Roswell Park Memorial Institute 1640 medium (RPMI 1640) supplemented with 10% fetal bovine serum (FBS, Gibco) and 1% penicillin–streptomycin solution.

Cell Imaging

Confocal imaging was carried out using 20 mm glass-bottom confocal dishes with cells incubated at 37 °C and 5% CO_2 for 24 h. Cell imaging was performed on a Zeiss LSM 780 confocal laser scanning microscope.

https://doi.org/10.1021/jacsau.3c00613
JACS Au 2023, 3, 3462–3472

Vivo Imaging

All animal procedures were conducted in accordance with Approval no. 20230220037 of the West China Hospital of Sichuan University and the Animal Ethics Committee on the protection of animals used in research. All mice were housed with a 12 h light/dark circadian cycle with ad libitum access to food and water. Vivo image was taken on an IVIS PerkinElmer Instruments.

■ ASSOCIATED CONTENT

Supporting Information

The Supporting Information is available free of charge at https://pubs.acs.org/doi/10.1021/jacsau.3c00613.

Detailed synthetic procedures; ^{1}H NMR, ^{13}C NMR, HRMS, absorption, and fluorescence data; and additional information as noted in the text, cell cytotoxicity, bioimaging data, and vivo imaging (PDF)

■ AUTHOR INFORMATION

Corresponding Author

Kun Li − *Key Laboratory of Green Chemistry and Technology of Ministry of Education, College of Chemistry, Sichuan University, Chengdu 610064, P. R. China;* orcid.org/0000-0002-8788-1036; Email: kli@scu.edu.cn

Authors

Hong Zhang − *Key Laboratory of Green Chemistry and Technology of Ministry of Education, College of Chemistry, Sichuan University, Chengdu 610064, P. R. China; Department of Radiology, West China Hospital, Sichuan University, Chengdu 610041, P. R. China*

Fei-Fan Xiang − *Key Laboratory of Green Chemistry and Technology of Ministry of Education, College of Chemistry, Sichuan University, Chengdu 610064, P. R. China*

Yan-Zhao Liu − *Key Laboratory of Green Chemistry and Technology of Ministry of Education, College of Chemistry, Sichuan University, Chengdu 610064, P. R. China*

Yu-Jin Chen − *Key Laboratory of Green Chemistry and Technology of Ministry of Education, College of Chemistry, Sichuan University, Chengdu 610064, P. R. China*

Ding-Heng Zhou − *Key Laboratory of Green Chemistry and Technology of Ministry of Education, College of Chemistry, Sichuan University, Chengdu 610064, P. R. China*

Yan-Hong Liu − *Key Laboratory of Green Chemistry and Technology of Ministry of Education, College of Chemistry, Sichuan University, Chengdu 610064, P. R. China*

Shan-Yong Chen − *Key Laboratory of Green Chemistry and Technology of Ministry of Education, College of Chemistry, Sichuan University, Chengdu 610064, P. R. China*

Xiao-Qi Yu − *Key Laboratory of Green Chemistry and Technology of Ministry of Education, College of Chemistry, Sichuan University, Chengdu 610064, P. R. China; Asymmetric Synthesis and Chiral Technology Key Laboratory of Sichuan Province, Department of Chemistry, Xihua University, Chengdu 610039, P. R. China;* orcid.org/0000-0003-1719-6137

Complete contact information is available at: https://pubs.acs.org/10.1021/jacsau.3c00613

Funding

This work was financially supported by the National Natural Science Foundation of China (nos. U21A20308 and 22077088) and the Foundation from Science and Technology Department of Sichuan Province (2022YFS0065).

Notes

The authors declare no competing financial interest.

■ ACKNOWLEDGMENTS

We also thank Yan-Hong Liu from the Comprehensive Training Platform of Specialized Laboratory, College of Chemistry, Sichuan University, for sample analysis.

■ REFERENCES

(1) Chen, H.; Liu, L.; Qian, K.; Liu, H.; Wang, Z.; Gao, F.; Qu, C.; Dai, W.; Lin, D.; Chen, K.; Liu, H.; Cheng, Z. Bioinspired large Stokes shift small molecular dyes for biomedical fluorescence imaging. *Sci. Adv.* **2022**, *8*, No. eabo3289.

(2) Hu, Z.; Fang, C.; Li, B.; Zhang, Z.; Cao, C.; Cai, M.; Su, S.; Sun, X.; Shi, X.; Li, C.; Zhou, T.; Zhang, Y.; Chi, C.; He, P.; Xia, X.; Chen, Y.; Gambhir, S. S.; Cheng, Z.; Tian, J. First-in-human liver-tumour surgery guided by multispectral fluorescence imaging in the visible and near-infrared-I/II windows. *Nat. Biomed. Eng.* **2019**, *4*, 259−271.

(3) Voskuil, F. J.; Steinkamp, P. J.; Zhao, T.; van der Vegt, B.; Koller, M.; Doff, J. J.; Jayalakshmi, Y.; Hartung, J. P.; Gao, J.; Sumer, B. D.; Witjes, M. J. H.; van Dam, G. M.; the SHINE study group. Exploiting metabolic acidosis in solid cancers using a tumor-agnostic pH-activatable nanoprobe for fluorescence-guided surgery. *Nat. Commun.* **2020**, *11*, 3257.

(4) Takahashi, R.; Ishizawa, T.; Inagaki, Y.; Tanaka, M.; Ogasawara, A.; Kuriki, Y.; Fujita, K.; Kamiya, M.; Ushiku, T.; Urano, Y.; Hasegawa, K. Real-time fluorescence imaging to identify cholangiocarcinoma in the extrahepatic biliary tree using an enzyme-activatable probe. *Liver Cancer* **2023**, 1−13.

(5) Zhang, H.; Shi, L.; Li, K.; Liu, X.; Won, M.; Liu, Y.-Z.; Choe, Y.; Liu, X.-Y.; Liu, Y.-H.; Chen, S.-Y.; Yu, K.-K.; Kim, J. S.; Yu, X.-Q. Discovery of an ultra-rapid and sensitive lysosomal fluorescence lipophagy process. *Angew. Chem., Int. Ed.* **2022**, *134*, No. e202116439.

(6) Chen, Y.; Wang, S.; Zhang, F. Near-infrared luminescence high-contrast in vivo biomedical imaging. *Nat. Rev. Bioeng.* **2023**, *1*, 60−78.

(7) Alander, J. T.; Kaartinen, I.; Laakso, A.; Pätilä, T.; Spillmann, T.; Tuchin, V. V.; Venermo, M.; Välisuo, P. A review of indocyanine green fluorescent imaging in surgery. *Int. J. Biomed. Imaging* **2012**, *2012*, 1−26.

(8) Usama, S. M.; Thapaliya, E. R.; Luciano, M. P.; Schnermann, M. J. Not so innocent: impact of fluorophore chemistry on the in vivo properties of bioconjugates. *Curr. Opin. Chem. Biol.* **2021**, *63*, 38−45.

(9) Owens, E. A.; Lee, S.; Choi, J.; Henary, M.; Choi, H. S. NIR fluorescent small molecules for intraoperative imaging. *WIREs Nanomed. Nanobiotechnol.* **2015**, *7*, 828−838.

(10) Wei, R.; Dong, Y.; Wang, X.; Li, J.; Lei, Z.; Hu, Z.; Chen, J.; Sun, H.; Chen, H.; Luo, X.; Qian, X.; Yang, Y. Rigid and photostable shortwave infrared dye absorbing/emitting beyond 1200 nm for high-contrast multiplexed imaging. *J. Am. Chem. Soc.* **2023**, *145*, 12013−12022.

(11) Dong, Y.; Lu, X.; Li, Y.; Chen, W.; Yin, L.; Zhao, J.; Hu, X.; Li, X.; Lei, Z.; Wu, Y.; Chen, H.; Luo, X.; Qian, X.; Yang, Y. Spectral and biodistributional engineering of deep near-infrared chromophore. *Chin. Chem. Lett.* **2023**, *34*, 108154.

(12) Bian, H.; Ma, D.; Pan, F.; Zhang, X.; Xin, K.; Zhang, X.; Yang, Y.; Peng, X.; Xiao, Y. Cardiolipin-targeted NIR-II fluorophore causes "Avalanche effects" for re-engaging cancer apoptosis and inhibiting metastasis. *J. Am. Chem. Soc.* **2022**, *144*, 22562−22573.

(13) Li, J.; Dong, Y.; Wei, R.; Jiang, G.; Yao, C.; Lv, M.; Wu, Y.; Gardner, S. H.; Zhang, F.; Lucero, M. Y.; Huang, J.; Chen, H.; Ge, G.; Chan, J.; Chen, J.; Sun, H.; Luo, X.; Qian, X.; Yang, Y. Stable, bright, and long-fluorescence-lifetime dyes for deep-near-infrared bioimaging. *J. Am. Chem. Soc.* **2022**, *144*, 14351−14362.

(14) Xu, Q.; Zhang, Y.; Zhu, M.; Yan, C.; Mao, W.; Zhu, W.-H.; Guo, Z. Bent-to-planar Si-rhodamines: a distinct rehybridization lights

up NIR-II fluorescence for tracking nitric oxide in the Alzheimer's disease brain. *Chem. Sci.* **2023**, *14*, 4091−4101.
(15) Fu, M.; Xiao, Y.; Qian, X.; Zhao, D.; Xu, Y. A design concept of long-wavelength fluorescent analogs of rhodamine dyes: replacement of oxygen with silicon atom. *Chem. Commun.* **2008**, 1780−1782.
(16) Koide, Y.; Urano, Y.; Hanaoka, K.; Piao, W.; Kusakabe, M.; Saito, N.; Terai, T.; Okabe, T.; Nagano, T. Development of NIR fluorescent dyes based on Si-rhodamine for in vivo imaging. *J. Am. Chem. Soc.* **2012**, *134*, 5029−5031.
(17) Grzybowski, M.; Taki, M.; Senda, K.; Sato, Y.; Ariyoshi, T.; Okada, Y.; Kawakami, R.; Imamura, T.; Yamaguchi, S. A highly photostable near-infrared labeling agent based on a phospha-rhodamine for long-term and deep imaging. *Angew. Chem., Int. Ed.* **2018**, *57*, 10137−10141.
(18) Chai, X.; Cui, X.; Wang, B.; Yang, F.; Cai, Y.; Wu, Q.; Wang, T. Near-infrared phosphorus-substituted rhodamine with emission wavelength above 700 nm for bioimaging. *Chem.—Eur. J.* **2015**, *21*, 16754−16758.
(19) Liu, J.; Sun, Y.-Q.; Zhang, H.; Shi, H.; Shi, Y.; Guo, W. Sulfone-rhodamines: a new class of near-infrared fluorescent dyes for bioimaging. *ACS Appl. Mater. Interfaces* **2016**, *8*, 22953−22962.
(20) Daly, H. C.; Matikonda, S. S.; Steffens, H. C.; Ruehle, B.; Resch-Genger, U.; Ivanic, J.; Schnermann, M. J. Ketone incorporation extends the emission properties of the xanthene Scaffold beyond 1000 nm†. *Photochem. Photobiol.* **2022**, *98*, 325−333.
(21) Chen, Y.-J.; Zhang, H.; Liu, Y.-Z.; Shi, L.; Xiang, F.-F.; Lin, R.-D.; Liu, Y.-H.; Chen, S.-Y.; Yu, X.-Q.; Li, K. Rational design of pH-independent and high-fidelity near-infrared tunable fluorescent probes for tracking leucine aminopeptidase in vivo. *ACS Sens.* **2023**, *8*, 2359−2367.
(22) Zhang, X.; Chen, L.; Huang, Z.; Ling, N.; Xiao, Y. Cyclo-ketal xanthene dyes: a new class of near-infrared fluorophores for super-resolution imaging of live cells. *Chem.—Eur. J.* **2021**, *27*, 3688−3693.
(23) Li, J.; Zhang, M.; Yang, L.; Han, Y.; Luo, X.; Qian, X.; Yang, Y. "Xanthene" is a premium bridging group for xanthenoid dyes. *Chin. Chem. Lett.* **2021**, *32*, 3865−3869.
(24) Lan, Q.; Yu, P.; Yan, K.; Li, X.; Zhang, F.; Lei, Z. Polymethine molecular platform for ratiometric fluorescent probes in the second near-Infrared window. *J. Am. Chem. Soc.* **2022**, *144*, 21010−21015.
(25) Vygranenko, K. V.; Poronik, Y. M.; Wrzosek, A.; Szewczyk, A.; Gryko, D. T. Red emissive sulfone-rhodols as mitochondrial imaging agents. *Chem. Commun.* **2021**, *57*, 7782−7785.
(26) Dejouy, G.; Laly, M.; Valverde, I. E.; Romieu, A. Synthesis, stability and spectral behavior of fluorogenic sulfone-pyronin and sulfone-rosamine dyes. *Dyes Pigm.* **2018**, *159*, 262−274.
(27) Li, N.; Wang, T.; Wang, N.; Fan, M.; Cui, X. A substituted-rhodamine-based reversible fluorescent probe for in vivo quantification of glutathione. *Angew. Chem., Int. Ed.* **2023**, *62*, No. e202217326.
(28) Emmert, S.; Quargnali, G.; Thallmair, S.; Rivera-Fuentes, P. A locally activatable sensor for robust quantification of organellar glutathione. *Nat. Chem.* **2023**, *15*, 1415−1421.
(29) Umezawa, K.; Yoshida, M.; Kamiya, M.; Yamasoba, T.; Urano, Y. Rational design of reversible fluorescent probes for live-cell imaging and quantification of fast glutathione dynamics. *Nat. Chem.* **2017**, *9*, 279−286.
(30) Wu, L.; Burgess, K. Fluorescent amino- and thiopyronin dyes. *Org. Lett.* **2008**, *10*, 1779−1782.
(31) Horváth, P.; Šebej, P.; Šolomek, T.; Klán, P. Small-molecule fluorophores with large Stokes shifts: 9-iminopyronin analogues as clickable tags. *J. Org. Chem.* **2015**, *80*, 1299−1311.
(32) Butkevich, A. N.; Lukinavičius, G.; D'Este, E.; Hell, S. W. Cell-permeant large Stokes shift dyes for transfection-free multicolor nanoscopy. *J. Am. Chem. Soc.* **2017**, *139*, 12378−12381.
(33) Kim, K. H.; Singha, S.; Jun, Y. W.; Reo, Y. J.; Kim, H. R.; Ryu, H. G.; Bhunia, S.; Ahn, K. H. Far-red/near-infrared emitting, two-photon absorbing, and bio-stable amino-Si-pyronin dyes. *Chem. Sci.* **2019**, *10*, 9028−9037.
(34) Kim, K. H.; Kim, S. J.; Singha, S.; Yang, Y. J.; Park, S. K.; Ahn, K. H. Ratiometric detection of hypochlorous acid in brain tissues of neuroinflammation and maternal immune activation models with a deep-red/near-infrared emitting probe. *ACS Sens.* **2021**, *6*, 3253−3261.
(35) Sarkar, S.; Lee, H.; Ryu, H. G.; Singha, S.; Lee, Y. M.; Reo, Y. J.; Jun, Y. W.; Kim, K. H.; Kim, W. J.; Ahn, K. H. A study on hypoxia susceptibility of organ tissues by fluorescence imaging with a ratiometric nitroreductase probe. *ACS Sens.* **2021**, *6*, 148−155.
(36) Shan, Y.-M.; Zhang, L.-N.; Wu, S.-X.; Li, X.-L.; Zhang, H.; Xiang, F.-F.; Yu, F.-Y.; Liu, Y.-H.; Yu, X.-Q.; Li, K.; Xu, W.-M.; Yu, K.-K. Revelation of β-galactosidase variation in senile sperms and organs via a silicon xanthene near-infrared probe. *Sens. Actuators, B* **2023**, *397*, 134663.
(37) Li, J.-M.; Xiang, F.-F.; Zhou, D.-H.; Xu, J.-X.; Zhang, H.; Liu, Y.-Z.; Kong, Q.-Q.; Yu, X.-Q.; Li, K. Rational design of near-infrared fluorescent probes for accurately tracking lysosomal viscosity with allyl snchoring Si-rhodamine. *Chem. Biomed. Imaging* **2023**.
(38) Zhang, L.-N.; Zhang, H.; Chen, S.-Y.; Liu, Y.-Z.; Yang, X.-H.; Xiang, F.-F.; Liu, Y.-H.; Li, K.; Yu, X.-Q. γ-glutamyltranspeptidase and pH based "AND" logic gate fluorescent probe for orthotopic breast tumor imaging. *Chem. Commun.* **2023**, *59*, 2795−2798.
(39) Lu, T.; Chen, F. Multiwfn: a multifunctional wavefunction analyzer. *J. Comput. Chem.* **2012**, *33*, 580−592.
(40) Zhang, J.; Lu, T. Efficient evaluation of electrostatic potential with computerized optimized code. *Phys. Chem. Chem. Phys.* **2021**, *23*, 20323−20328.
(41) Bharadwaj, A.; Bydoun, M.; Holloway, R.; Waisman, D. Annexin A2 heterotetramer: structure and function. *Int. J. Mol. Sci.* **2013**, *14*, 6259−6305.
(42) Lokman, N. A.; Ween, M. P.; Oehler, M. K.; Ricciardelli, C. The role of annexin A2 in tumorigenesis and cancer progression. *Cancer Microenviron.* **2011**, *4*, 199−208.
(43) Díaz, V. M.; Hurtado, M.; Thomson, T. M.; Reventós, J.; Paciucci, R. Specific interaction of tissue-type plasminogen activator (t-PA) with annexin II on the membrane of pancreatic cancer cells activates plasminogen and promotes invasion in vitro. *Gut* **2004**, *53*, 993−1000.
(44) Mai, J.; Waisman, D. M.; Sloane, B. F. Cell surface complex of cathepsin B/annexin II tetramer in malignant progression. *Biochim. Biophys. Acta* **2000**, *1477*, 215−230.
(45) Sharma, M. R.; Koltowski, L.; Ownbey, R. T.; Tuszynski, G. P.; Sharma, M. C. Angiogenesis-associated protein annexin II in breast cancer: selective expression in invasive breast cancer and contribution to tumor invasion and progression. *Exp. Mol. Pathol.* **2006**, *81*, 146−156.
(46) Shiozawa, Y.; Havens, A. M.; Jung, Y.; Ziegler, A. M.; Pedersen, E. A.; Wang, J.; Wang, J.; Lu, G.; Roodman, G. D.; Loberg, R. D.; Pienta, K. J.; Taichman, R. S. Annexin II/annexin II receptor axis regulates adhesion, migration, homing, and growth of prostate cancer. *J. Cell. Biochem.* **2008**, *105*, 370−380.
(47) Jaiswal, J. K.; Lauritzen, S. P.; Scheffer, L.; Sakaguchi, M.; Bunkenborg, J.; Simon, S. M.; Kallunki, T.; Jäättelä, M.; Nylandsted, J. S100A11 is required for efficient plasma membrane repair and survival of invasive cancer cells. *Nat. Commun.* **2014**, *5*, 3795.
(48) Shen, D.; Xu, B.; Liang, K.; Tang, R.; Sudlow, G. P.; Egbulefu, C.; Guo, K.; Som, A.; Gilson, R.; Maji, D.; Mondal, S.; Habimana-Griffin, L.; Akers, W. J.; Li, S.; Liu, Y.; Bloch, S.; Kurkure, S.; Nussinov, Z.; Seidel, A.; Tsen, S.-W. D.; Achilefu, S. Selective imaging of solid tumours via the calcium-dependent high-affinity binding of a cyclic octapeptide to phosphorylated annexin A2. *Nat. Biomed. Eng.* **2020**, *4*, 298−313.
(49) Zhang, P.; Huang, H.; Chen, Y.; Wang, J.; Ji, L.; Chao, H. Ruthenium(II) anthraquinone complexes as two-photon luminescent probes for cycling hypoxia imaging in vivo. *Biomaterials* **2015**, *53*, 522−531.

https://doi.org/10.1021/jacsau.3c00613
JACS Au 2023, 3, 3462−3472